ROYAL SOCIETY
OF CHEMISTRY

PAPER

Check for updates

A facile synthesis of high entropy alloy nanoparticle–activated carbon nanocomposites for synergetic degradation of methylene blue

Yuyu Liu,[a] Zheng Chen, [ID] *[a] Xiaoqin Yang,[a] Jinyong Zhang, [ID] [a] Zhonggang Sun,[b] Yuzeng Chen[c] and Feng Liu[c]

Nanocomposites of CoCrFeMnNi high entropy alloy nanoparticle–activated carbon (HEA NPs–AC) were prepared by a facile and controllable impregnation–adsorption method. The HEA NPs–AC showed excellent catalytic performance in the degradation of methylene blue (MB) without any peroxide addition. Besides, their reaction rate is also competitive among single-element and other catalysts. The outstanding efficiency is attributed to the coupling effects of the solid-solution structure of HEA NPs, and the large specific surface area and substantial reaction channels of AC. Moreover, the HEA NPs embedded in distinctive porous architectures accelerate the electron transfer and the mass transport as nanoscale galvanic cells in active bond breaking of MB. The nanocomposites of HEA NPs–AC are distinguished by containing non-noble metals and having high catalytic performance due to the synergetic degradation, providing a better alternative for efficient metal catalysis.

1. Introduction

High entropy alloys (HEAs) are composed of equiatomic or near-equiatomic mixing of multiple elements rather than the conventional single major composition. Tremendous advances have been achieved since this new class of metallic material was proposed in the last decade.[1–5] Recently, high entropy alloy nanoparticles (HEA NPs) have become one of the research frontiers for overcoming the difficulty of mixing elements with vastly different chemical and physical properties.[6] It is creative to downsize bulk HEAs to HEA NPs which shows greatly prospective candidates for a wide range of applications in catalysis,[7,8] energy storage,[9] superparamagnetic and super-conducting materials.[10] Löffler et al.[11] have reported that a surprisingly high intrinsic activity of the multinary CrMnFe-CoNi NPs is at least comparable to that of Pt NPs under the same conditions. Furthermore, HEA NPs prepared by the car-bothermal shock method can realize 100% conversion of ammonia and ultrahigh selectivity toward nitrogen oxide.[6] These encouraging works reveal remarkable catalytic perfor-mance of HEA NPs, which inspires us to broaden its application for synthetic dye degradation.

Currently, the methods of azo dye degradation are various including photocatalysis, redox reduction, and Fenton-like reaction. Visible light photocatalysis could offer an eco-friendly alternative for the selective transformation of organic molecules.[12] Photocatalysis is generally supposed to be the catalysis of a photochemical reaction at a solid surface, espe-cially a semiconductor such as TiO_2, $BaTiO_3$, Ag_2O, etc.13–16 The factor of light is indispensable for titanium dioxide via photocatalytic decomposition of pollutants due to photo-generated holes and photogenerated electrons. Han et al. developed an alveoli-like bilayer Janus membrane as a highly efficient dye-sensitized photocatalyst with fluorescence peak at around 682 nm for water purification under visible light irra-diation and photosensitizer decoration for tetracycline was up to 36%.[17] The methods of redox reduction and Fenton-like reaction for azo dye degradation are different from photo-catalysis due to the insensitivity of HEA powders, Fe-based metallic glasses, and magnetite nanoparticles to solar light. Fe-based metallic glasses have been firstly investigated for dyes decomposition and mineralization via Fenton-like process due to its far-from-equilibrium states, chemical homogeneity, and random atomic packing.[18,19] However, highly efficient advanced oxidation processes are limited by many parameters, such as strong acid environments and peroxides that may induce secondary contamination. What's more, ball-milled HEA powders present good performance in the decoloration of azo dye (Direct Blue 6) as well,[20,21] while the difficulty in recovering the powder seriously limits its industrial application. Never-theless, porous carbon shows particularly distinguishing features with network geometry, co-existing of microstructure

[a]School of Material Science and Engineering, China University of Mining and Technology, Xuzhou, Jiangsu 221008, China. E-mail: chenzheng1218@163.com; xiaoqinyang0530@163.com; Fax: +86 516 83591870; Tel: +86 516 83897715

[b]Tech Institute for Advanced Materials, College of Materials Science and Technology, Nanjing Tech University, Nanjing, 210009, China

[c]State Key Laboratory of Solidification Processing, Northwestern Polytechnical University, Xi'an, Shaanxi 710072, China
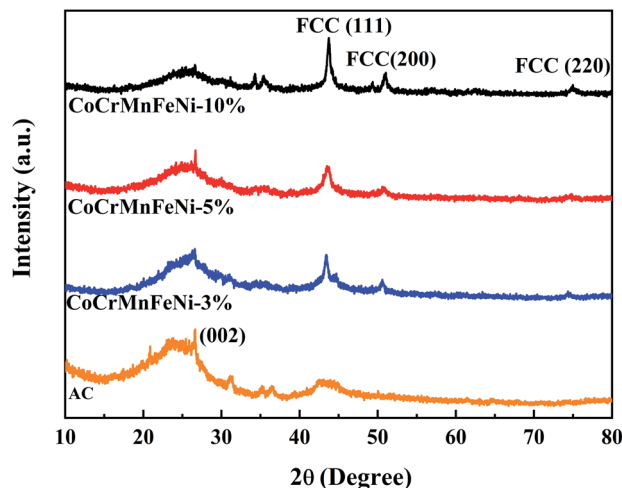
Fig. 1 XRD patterns of CoCrFeMnNi HEA NPs–AC with different loadings (0 wt%, 3 wt%, 5 wt%, and 10 wt%).

and mesostructure, high specific surface area, and convenience for nitrogen-doping.[22–24] HEA NPs loaded on carbon nanostructures have attracted growing attention due to its distinctive structures and extensive application prospects in energy conversion and storage, and heterogeneous catalysis.[25,26]

In this work, a facile impregnation–adsorption method was utilized to fabricate noble metal-free CoCrFeMnNi HEA NPs and single-element NPs loaded on activated carbon (AC). The lattice structure and specific surface area of HEA NPs–AC were discussed in detail. In addition, the microstructure, morphology and electronic valence state were featured to reveal the stability and activity of NPs. To evaluate catalytic performance, the as-prepared nanocomposites were used for synthetic dye degradation *via* redox process to cleave active bonds. Finally, the mechanism of dye degradation and possible fracture pathways of active bonds were illustrated.

2. Experimental

The nanocomposites of HEA NPs–AC were fabricated by a simple impregnation–adsorption method just *via* the precursor solution absorption and calcination. The initial precursor included cobalt nitrate hexahydrate ($Co(NO_3)_2\cdot6H_2O$), chromic nitrate nonahydrate ($Cr(NO_3)_2\cdot9H_2O$), manganese nitrate tetrahydrate ($Mn(NO_3)_2\cdot4H_2O$), Aluminum nitrate nonahydrate ($Al(NO_3)_3\cdot9H_2O$), ferric nitrate non-ahydrate ($Fe(NO_3)_3\cdot9H_2O$), nickel nitrate hexahydrate ($Ni(NO_3)_2\cdot6H_2O$), and ethanol (AR grade), which were employed to prepare precursor solution. Commercially available AC was firstly crushed to 20–40 mesh and then cleaned with ultrasonic shock in deionized water, followed by filtration and drying at 323 K for 36 h as carbon supports. The quantitative metal-nitrates of CoCrFeMnNi were respectively dissolved in 50 mL ethanol as precursor solutions that were designed for equal
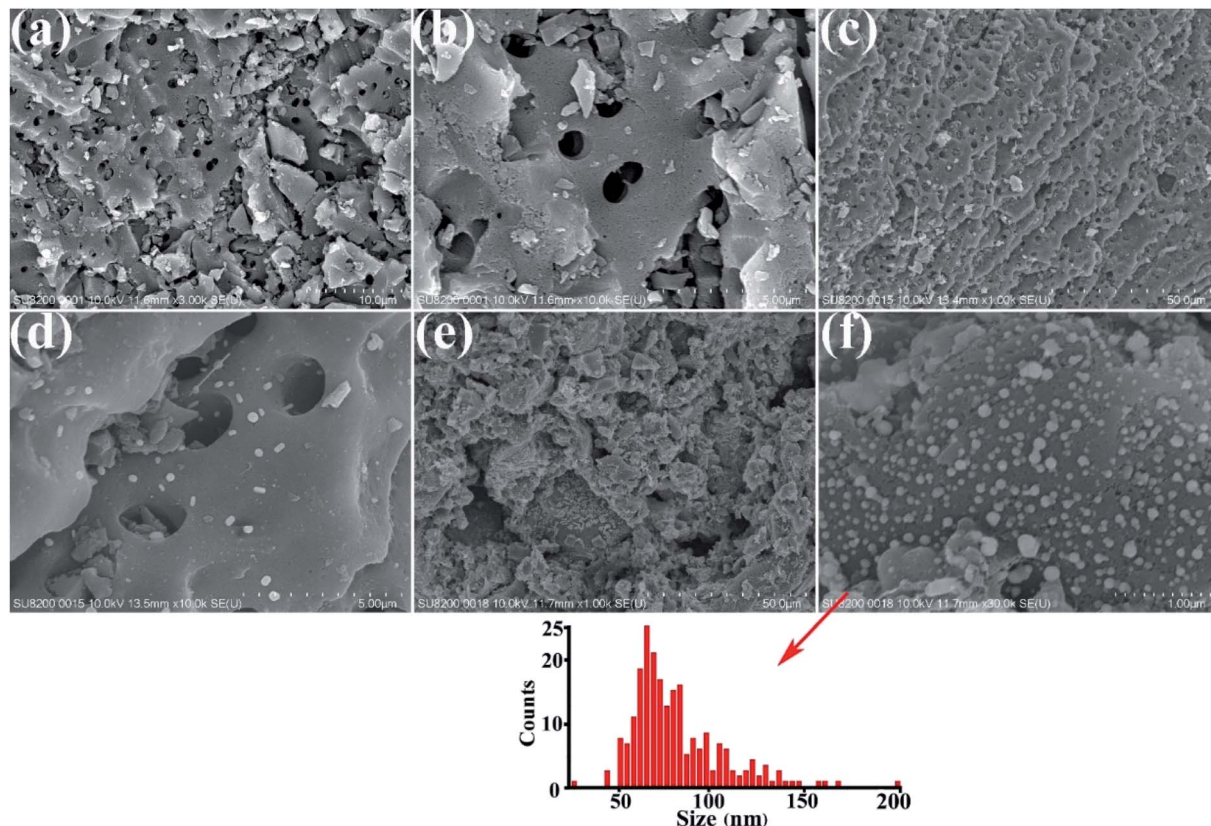

Fig. 2 Microstructures of the HEA NPs–AC and AC. (a) and (b) non-loaded AC, (c) and (d) 3 wt% CoCrFeMnNi HEA NPs–AC, (e) and (f) 10 wt% CoCrFeMnNi HEA NPs–AC with the inset of the statistical size distribution of NPs which shows the average diameters of 89 nm respectively.
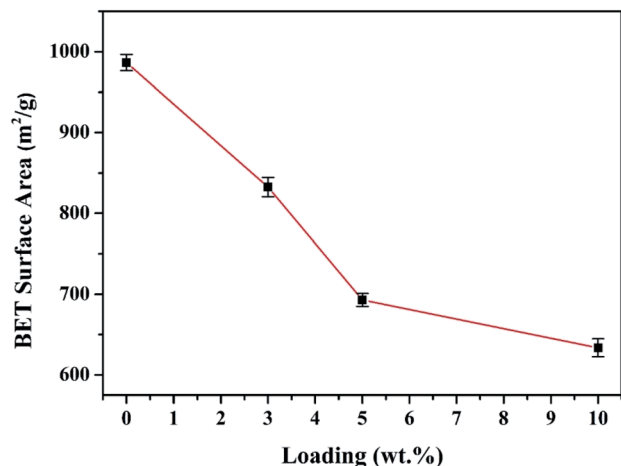
Fig. 3 Comparison of the measured BET specific surface area ($m^2 g^{-1}$) with different loadings of the CoCrFeMnNi NPs–AC.

where m_{metal} is the mass of loaded HEA, m_{AC} is the mass of AC. The washed AC (3 g) was dipped into the precursor solutions of mixed metal salts for 4 h. Then excess ethanol was removed by rotary evaporator at 313 K for 40 min and the obtained AC was left to dry at room temperature. The ethanol-based precursor solution benefited uniform loading and particle dispersion as a result of favorable wettability to carbon. The precursor-loaded AC was placed into the quartz tube of the furnace and then the furnace was pumped into the vacuum. Protective gas (volume ratio of Ar : H_2, 95% : 5%) was subsequently introduced into the furnace with heating to 1273 K for 3 h, and then cooling to room temperature.

The Brunauer–Emmett–Teller (BET) surface area analysis of the catalysts was performed using the nitrogen adsorption method (ASAP2020Plus). Microstructural morphologies of the samples were characterized by a scanning electron microscope (SEM, Hitachi SU8220) and a high-resolution transmission electron microscope (HRTEM, Tecnai G2 F20). Compositional information and EDS maps of the microstructures were measured in a scanning transmission electron microscope equipped with high angle annular dark field detectors (HAADF-STEM, FEI Talos F200s TEM/STEM). Chemical composition and valence state of the samples were characterized using an X-ray photoelectron spectroscopy

atomic ratio, while the total theoretical loading of AC was various (3 wt%, 5 wt%, and 10 wt%):

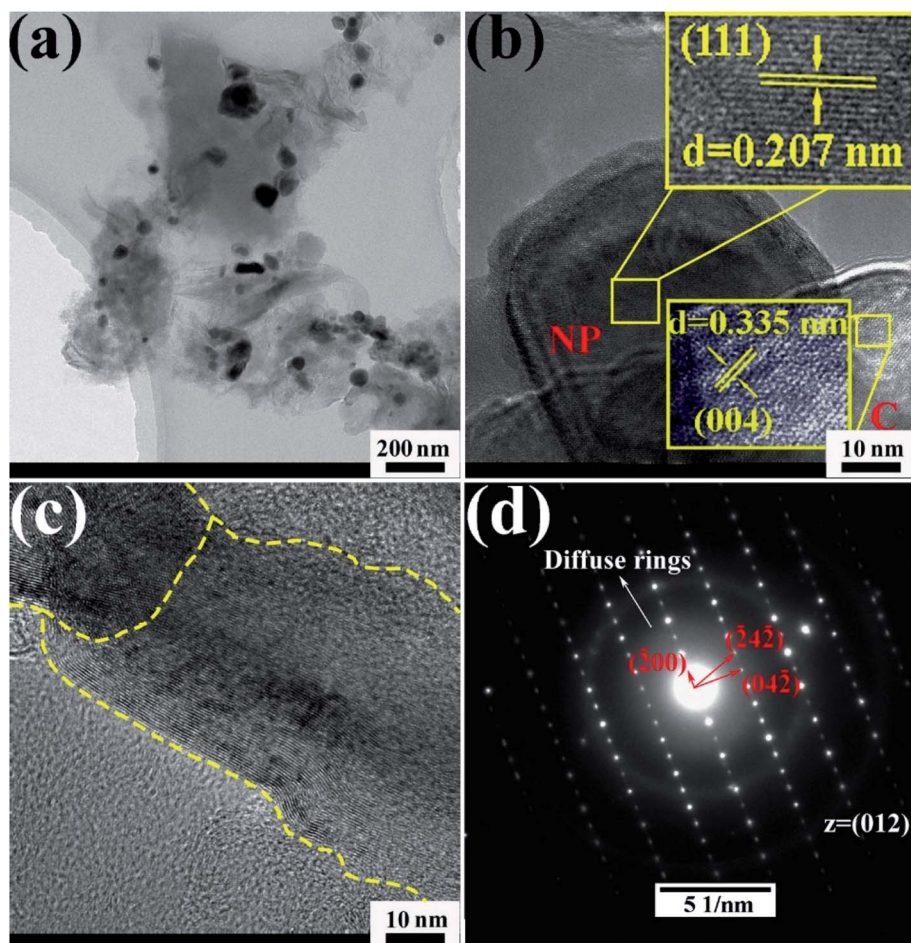$$\text{Loading} = \frac{m_{metal}}{m_{metal} + m_{AC}} \times 100 \ \ \text{wt\%}$$

Fig. 4 (a–c) HRTEM images of 10 wt% CoCrFeMnNi HEA NPs–AC with different magnification, (d) SAED pattern.

(XPS, ESCALAB 250Xi). Atomic structure and phase were revealed by X-ray diffractometer (XRD, Bruker D8 ADVANCE) with Cu Kα radiation operating at 40 kV and 40 mA. High-resolution mass spectra (HRMS, Q EXTRACTIVE) was employed to detect functional groups of dye solution after degradation. The total organic carbon (TOC) results of MB dye mineralization were obtained by a TOC analyzer (TOC-5000, Shimadzu). Fourier transform infrared spectroscopy (FT-IR, Bruker Vertex 80v) of CoCrMnFeNi NPs/AC before and after decomposition were recorded in the spectral range 4000 to 500 cm^{-1}.

The as-prepared nanocomposites of HEA NPs–AC were added into methylene blue (MB, $C_{16}H_{18}ClN_3S \cdot 3H_2O$, AR grade) solution of 100 mL (catalyst dosage of 4 g L^{-1}, dye concentration of 200 ppm, and constant temperature of 298 K, if not specifically mentioned). In the process of degradation, the reaction solution was stirred at a fixed speed and taken out of 2 mL at a selected time. The sucked solutions were centrifuged at a speed of 13 000 rpm and then determined by ultraviolet visible spectrophotometer (UV-vis) to obtain the absorbance spectrum.

3. Results and discussion

3.1 Microstructure of the CoCrFeMnNi HEA NPs–AC

XRD patterns of the CoCrFeMnNi HEA NPs–AC with different loadings are shown in Fig. 1. The result of AC demonstrates that there are broad and amorphous diffraction peaks at 22°–26° and 42°–45° with (002) planes (2θ = 26.5°). The sharply crystallized peaks are the HEA NPs. The intensity of peaks heightens

gradually with loading from 3 wt% to 10 wt% in Fig. 1. The crystalline peak (2θ = 43.7°) assigned to (111) plane without splitting is the multicomponent face-centered cubic (FCC) phase for 10 wt% CoCrFeMnNi HEA NPs–AC. The peaks at 50.9° and 74.9° correspond to (200) and (220), respectively.

SEM images of the HEA NPs–AC and AC are exhibited in Fig. 2. Fig. 2a and b display a smooth surface of non-loaded AC with no impurity substance and few AC exfoliations after high temperature calcination. The circular-like macropores are abundantly distributed on the surface and form a developed porosity framework. The microstructure of 3 wt% sample begins to change with NPs appearing on the surface and the macropores channels in Fig. 2c and d. Nevertheless, Fig. 2e and f show that the morphology of pores seems to collapse and merge into unlike the former and large amounts of CoCrFeMnNi HEA NPs uniformly disperse with an average diameter of 89 nm in the inset of the statistical size distribution. Specific surface area of different loadings for CoCrFeMnNi NPs–AC are shown in Fig. 3. The S_{BET} of 3–10 wt% samples is lower than that of AC (968.48 m^2 g^{-1}) and decreases with the increase of loading because the reduced S_{BET} provides more space for the growth of the HEA NPs. Though the loading of the HEA NPs leads to the pore collapse of AC and reduction of S_{BET}, the collapses facilitate the formation of massive reaction channels, which provides an effect route of reactants and dye molecule contacting the HEA NPs.[27] It also improves catalytic efficiency through an effective pre-adsorption of organic molecules. Satisfied catalytic
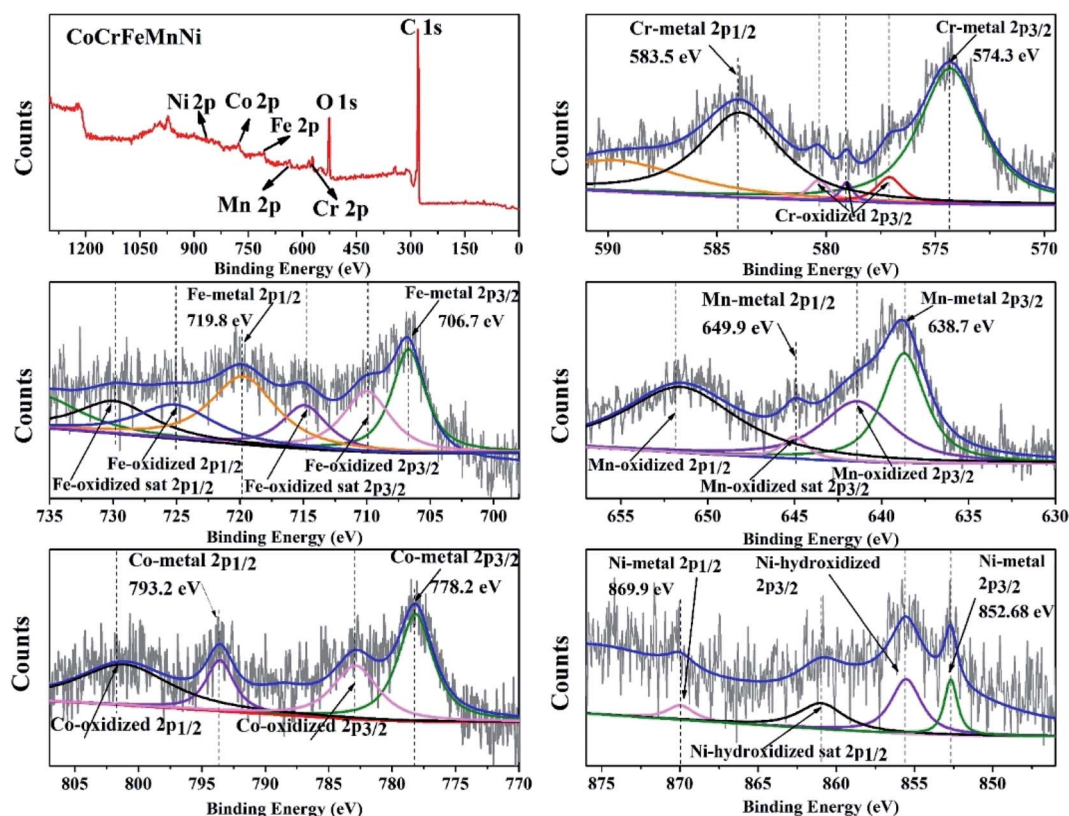

Fig. 5 Characteristic XPS peaks of the10 wt% CoCrFeMnNi HEA NPs with individual element of Cr, Fe, Mn, Co and Ni.

performance demands large specific surface area and massive active sites of the HEA NPs.

TEM images of the CoCrFeMnNi HEA NPs are illustrated in Fig. 4. The inter-planar spacing of the lattice planes is 0.207 nm in Fig. 4b, which is in agreement with the (111) plane of FCC metal crystal phase (Fig. 1). The inter-planar spacing is measured to be 0.335 nm corresponding to (002) plane of carbon. The yellow line in Fig. 4c mainly emphasizes long-range disordering of carbon which conforms to the broad peak in Fig. 1 and amorphous diffuse rings in Fig. 4d. Different region outlined by yellow line shows different orientation that means many defects. XRD patterns are characterized with intrinsic feature and the same situation as described in Fig. 4c is common. SAED image in Fig. 4d shows amorphous diffuse rings of carbon and FCC structure of CoCrFeMnNi HEA with (012) zone axis.

3.2 Chemical composition of the CoCrFeMnNi HEA NPs

In order to obtain the information of electronic structure for transition metal HEA NPs, XPS spectra and characteristic peaks of the individual element are presented in Fig. 5. The peaks of C_{1s}, O_{1s}, Co_{2p}, Cr_{2p}, Mn_{2p}, Fe_{2p} and Ni_{2p} are observed in full range pattern. The binding energies of the CoCrFeMnNi NPs at 778.2 eV, 574.3 eV, 638.7 eV, 706.7 eV and 852.68 eV are characterized for Co, Cr, Mn, Fe, and Ni, which reveals that quinary metal elements are in zero valence state in Fig. 5. While XPS results also show few fitting peaks of mixed metallic bonding and slightly oxidized bonding states due to inadequate reduction reaction and oxidation in the air, especially for the non-noble metals.

As displayed in Fig. 6, the morphology and elemental maps of the CoCrFeMnNi NPs were featured by HAADF-STEM. The as-synthesized HEA NPs in Fig. 6a and b are nearly spherical in shape dispersing on the carbon supports. STEM EDS elemental maps of individual HEA NP reveal that the distribution of elements is uniform while the counterpart of Cr and Mn is relatively less due to the low vapor pressure. The quantificational composition ratio of CoCrFeMnNi NPs for individual element are 17.08 at%, 9.77 at%, 29.15 at%, 15.75 at% and 28.25% respectively in Fig. 6c. EDS line-scanning result in Fig. 6d for a another HEA NP visually displays the elemental distribution that is roughly same as Fig. 6c.

3.3 Degradation performance of the as-prepared nanocomposites of HEA NPs–AC

Normalized concentrations of the MB solution are obtained (depending on the chromogenic group peak at 291 nm) as shown in Fig. 7a. According to UV-vis absorbance results, it takes twelve minutes for 10 wt% CoCrFeMnNi NPs–AC to reduce dye concentration to less than 15% via redox reduction, while
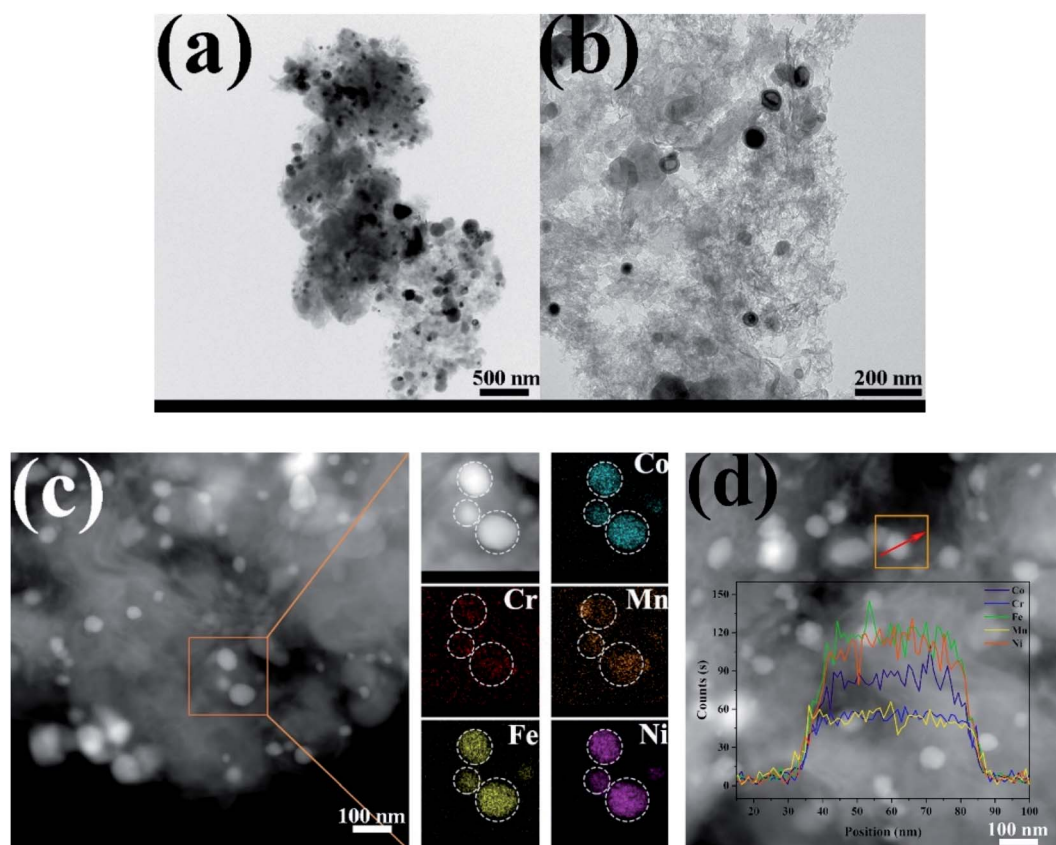

Fig. 6 (a) and (b) TEM morphology of the 10 wt% CoCrFeMnNi HEA NPs–AC, (c) HAADF image and STEM elemental maps of the 10 wt% CoCrFeMnNi HEA NPs–AC, (d) EDS line-scanning of the 10 wt% CoCrFeMnNi HEA NPs–AC.
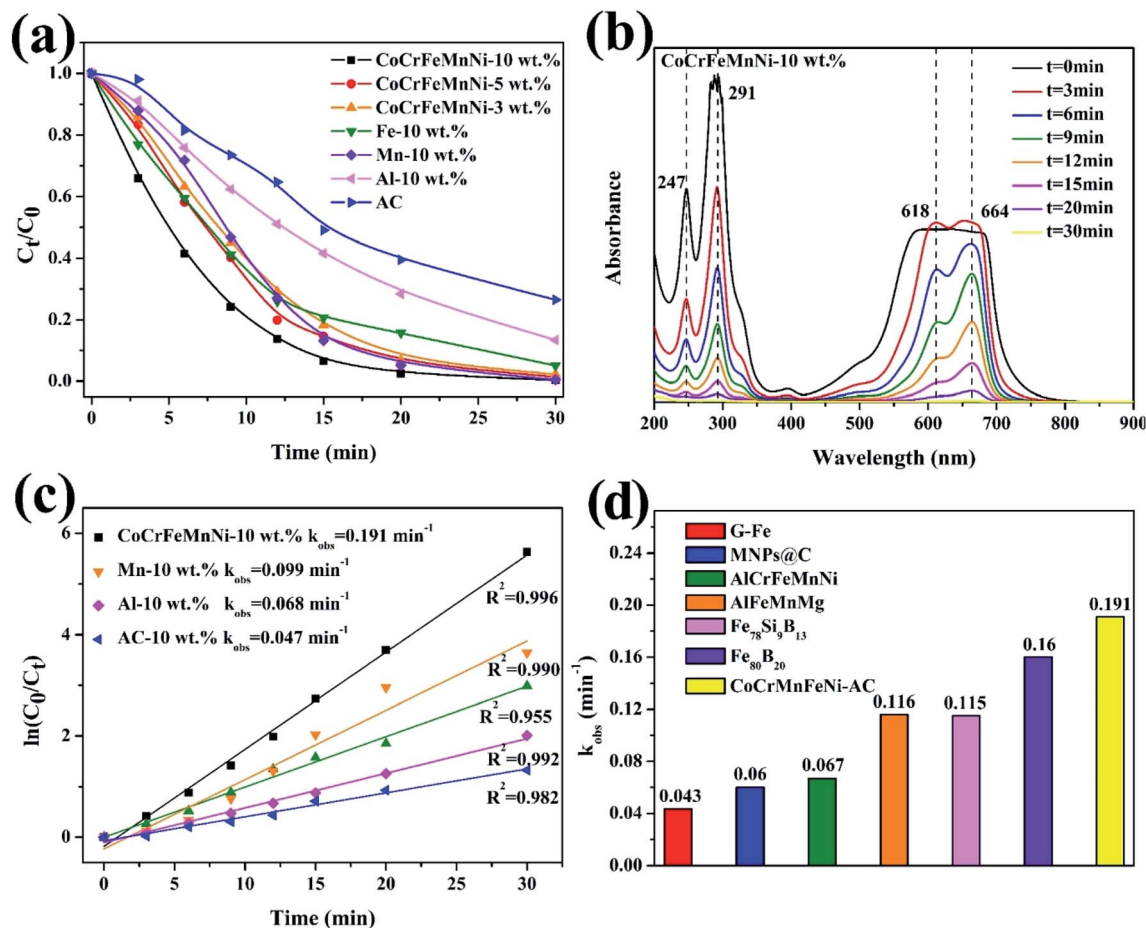
Fig. 7 (a) Normalized concentrations with the peak intensity at 291 nm as a function of degradation time for different types catalysts, (b) UV-vis absorbance spectra of the MB solutions at different time intervals for 10 wt% CoCrFeMnNi HEA NPs−AC, (c) the $\ln(C_0/C_t)$ vs. time curves for 10 wt% CoCrAlFeNi HEA NPs−AC, single element NPs−AC and AC, (d) comparison of the reaction rates (k_{obs}) among different catalysts.

AC as catalyst shows an almost linear and sluggish adsorption curve. The decomposition efficiency of single-element NPs for Mn, Fe, and Al is slower than that of multicomponent catalysts owing to the lack of high entropy effects. Furthermore, the increase of loading (from 3 wt% to 10 wt%) can result in more generation of the NPs and consequent more exposure of active sites to accelerate degradation. The UV-vis spectrums in Fig. 7b demonstrate the effective degradation of the MB, the breakage and conversion of chemical bonds over loaded and non-loaded catalysts compared with AC. Four absorption peaks are observed at 247 nm, 291 nm, 618 nm and 664 nm approximately in MB solutions. The peaks at 247 nm and 291 nm stem from triazine groups. Besides, auxochrome and chromophore groups are the other two peaks at 618 nm and 664 nm.[28]

The dye degradation efficiency of an environmental catalyst is reflected by the value of reaction. The comparable results about other catalysts for decomposition are summarized in Table 1. The reaction rates (k_{obs}) can be fitted by the pseudo-first-order kinetic model, $\ln(C_0/C_t) = k_{obs}t$, where C_0 is the initial concentration of dye at $t = 0$ and C_t is the dye

Table 1 Comparison of the reaction rates (k_{obs}) among different catalysts

Catalysts	Organic dye	Concentration (ppm)	Dosage (g L^{-1})	k_{obs} (min^{-1})	Ref.
G-Fe	Direct Blue 6	200	13.4	0.043	39
MNPs@C	Industrial wastewater	800	5	0.06	40
AlCrFeMnNi	Direct Blue 6	200	0.5	0.067	21
AlFeMnMg	Direct Blue 6	200	0.5	0.116	21
Fe$_{78}$Si$_9$B$_{13}$	Acid orange II	200	13.3	0.115	41
Fe$_{80}$B$_{20}$	Direct Blue 6	200	13.3	0.160	42
CoCrFeMnNi−AC	Methylene blue	200	4	0.191	This work

concentration at time t. Fig. 7c shows that the order of decomposition efficiency for these catalysts is as follow: CoCrFeMnNi > Fe > Mn > Al > AC. The comparison of the reaction rates (k_{obs}) among zero value metals, MNPs@C, ball-milled HEA, and metallic glass indicates that CoCrFeMnNi NPs–AC have surprisingly high intrinsic activity and competitive catalytic performance in Fig. 7d and Table 1. Deekshitha et al. prepared AgO/Ag$_2$O@TiO$_2$ with a reduction of Photoluminescence intensity on decorating TiO$_2$@Ag$_2$O-nanoparticle to degrade Reactive Blue 220 dye completely (100 ppm, 5 g L^{-1}) under visible light irradiation in 60 min.[14] Compared with

photocatalysis, HEA NPs present superior catalytic performance as well.

As shown in Fig. 8a and b, the non-loaded AC after degradation retains the analogously original morphological structure like Fig. 3a and b with no intermediates or decomposition products adhering to carbon supports. However, massive cotton-like sediments are around CoCrFeMnNi HEA NPs in Fig. 8c and d, which dramatically differ from those of carbon. The degradation products are similar to that of Fe-based amorphous powder and ball-milled HEA for organic dye degradation indicated by Wang et al. and Wu et al.[21,29] XRD
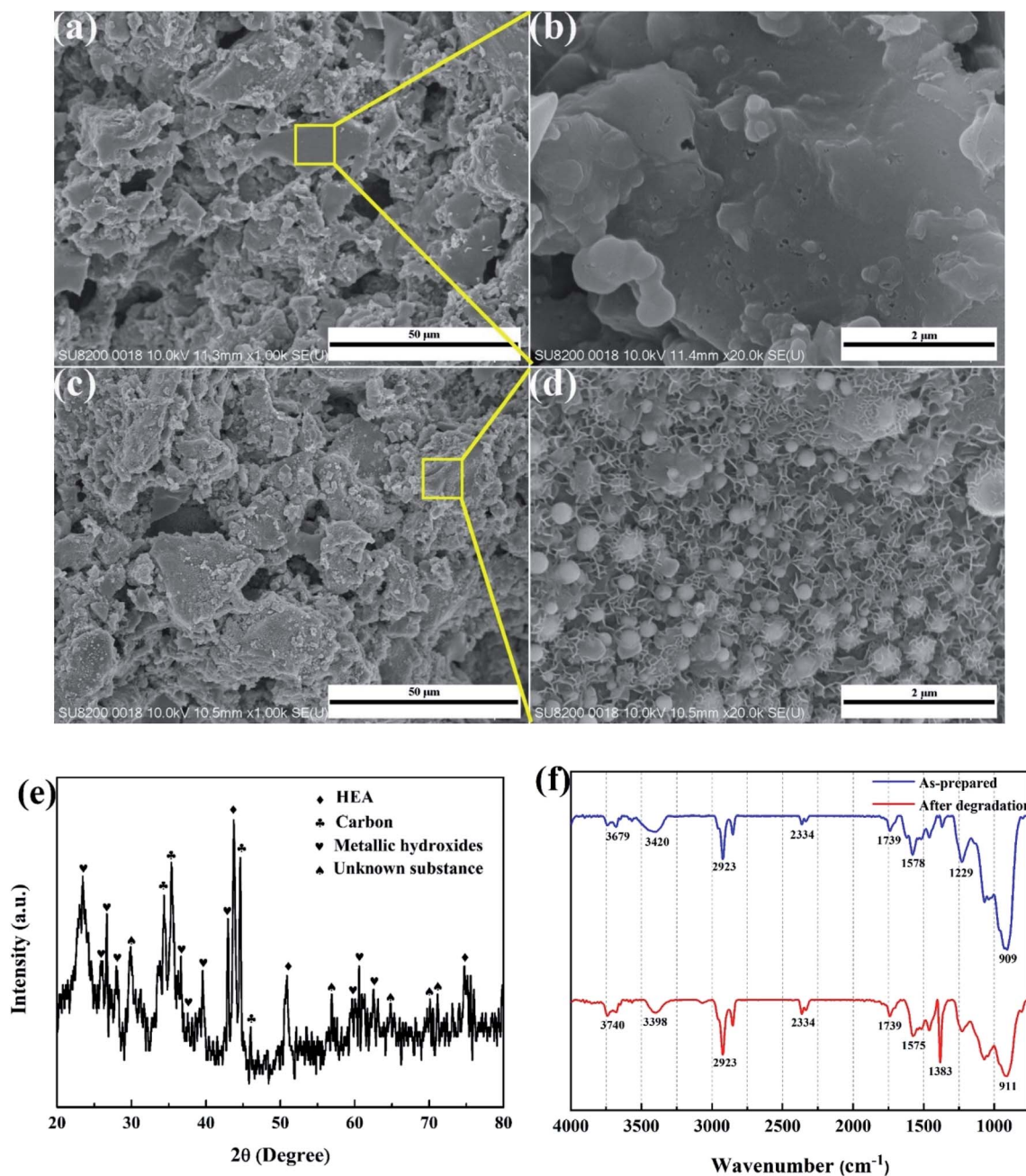

Fig. 8 Microstructures of the CoCrFeMnNi HEA NPs–AC and AC after MB dye decomposition. (a) and (b) non-loaded AC, (c) and (d) 10 wt% CoCrFeMnNi HEA NPs–AC, (e) XRD pattern of catalyst after degradation, (f) FT-IR spectra of as-prepared and after-degradation sample.
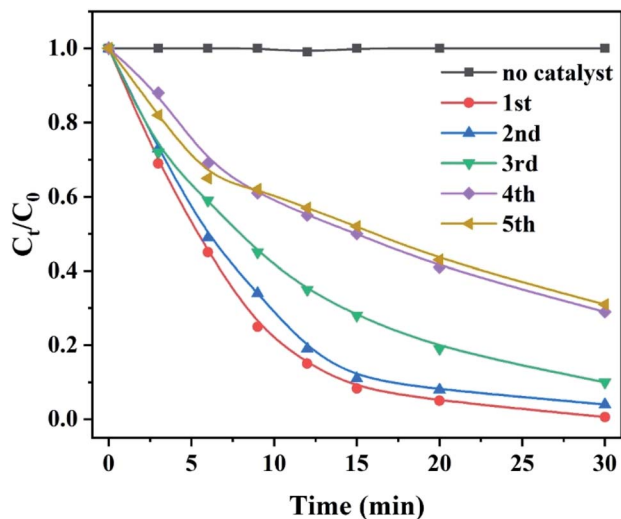
© 2021 The Author(s). Published by the Royal Society of Chemistry

Fig. 9 Reusability of 10 wt% CoCrFeMnNi HEA NPs–AC catalysts for MB degradation.

result in Fig. 8e remains FCC phase of HEA NPs and shows multiple metallic hydroxides which are generated by the combination of metallic ions and hydroxyl ions during degradation. The nanoscale surface features provided more active sites for the reaction to proceed and thus improved the degradation efficiency. Moreover, the surface of the HEA NPs uncovered by the decomposed products is still smooth without apparent corrosion pits, which demonstrates the stability and strong catalytic ability of the HEA NPs in the degradation process. The typical redox reaction is responsible for the zero valent metal degradation of dyes.[30,31] However, HEA NPs are superior to conventional single or binary component in catalysis.

It is reported that the functional groups of MB around 2923 and 2852 cm^{-1} correspond to C–H stretching of –CH_3 and –CH_2. The absorption peaks around 1383 cm^{-1} are attributed to the presence of –COOH group.[32] As shown in Fig. 8f, the intensity of the peaks at 2923 and 1383 cm^{-1} increases for the post-degradation sample due to a few undegraded and residual MB dye. The FT-IR spectra of other peaks remain consistent compared to as-prepared sample and post-degradation sample which means the stability of the catalyst. The sustainability and stability of the outstanding catalyst is a critically precious in environmental pollutants remediation. Fig. 9 demonstrates the reusability of 10 wt% CoCrFeMnNi HEA NPs–AC catalysts for MB degradation. The previous three cycles present satisfied decomposition performance and the efficiency of other cycles begins to decay but still sustained at nearly 75%.

With the increase of reaction time, the macromolecule MB (m/z = 284.1) in Fig. 10a is firstly initiated by fracture of chromophore center, and then cracked into smaller molecules (m/z = 154.1, and 168.2) at different time in Fig. 10b–d, which are in agreement with the above UV-vis analysis in Fig. 7b. The relative abundance of m/z = 284.1 at different time gradually decreases with increasing degradation time in Fig. 10e. Two possible decomposition pathways of the MB are speculated, according to

the m/z peaks of 154 and 168 as shown in Fig. 10g. The other two reaction intermediate products are not detected, probably due to that they are further decomposed into smaller molecules. It is also reported that the azo bond '–C=N–' is reduced into '–NH_2' by reducing agents firstly, then hydrogen ions and electrons that combine with broken dye molecules are generated between metals.[33] Moreover, the TOC removal of MB dye increases with degradation time and the TOC can be more than 50% at 30 min with nearly 100% decoloration in Fig. 10f.

3.4 Synergetic degradation mechanism of the CoCrFeMnNi HEA NPs–AC

Fig. 11 shows the schematic diagram for catalytic reaction mechanism of the MB for CoCrFeMnNi HEA NPs–AC. The as-synthesized sample with convenient preparation, large specific surface area and uniform distribution are expected to have promising applications for environmental catalysts. Therefore, the noble metal-free HEA NPs and single-element NPs supported by carbon were employed as heterogeneous catalysts to evaluate catalytic performance of dye water degradation.

3.4.1. HEA solid-solution phase of the NPs. The CoCrFeMnNi HEA NPs prepared by the impregnation–adsorption method consist of FCC phases with homogeneous elements distribution, as shown in Fig. 1, 2 and 4–6. Owing to the intrinsic characteristics of HEA, the solid-solution phase is provided with homogeneous distribution of constituents which plays a crucial role in outstanding catalytic effect. Yao *et al.*[6] deemed that HEA NPs with highly homogenous solid-solution were more likely to enhance catalytic selectivity. Although the simple solid-solution phases in HEAs can be identified, atomic arrangements are complex due to their random or quasi-random atomic occupancies of the multiple principal elements. Therefore, the atomic-size effect in multicomponent crystalline lattices induces to lattice distortion and strain energy, and the new active site configurations appears which produces potentially excellent catalytic properties.[28–34] Above all, the well-distributed compositions induce substantial numbers of new active site configurations with different constitutions of neighboring atoms electronically interacting with each other.[29–36] The similar properties have been confirmed that CoCrFeMnNi HEA NPs are more active and sensitive than quaternary or binary subsystems, implying comparable intrinsic activity of the noble metal-free multinary alloy as the state-of-art oxygen reduction reaction catalyst.[11]

3.4.2. Specific surface area. It was confirmed that the large specific surface area favored the substantial formation of the HEA NPs (Fig. 3 and 11). The synergistic coordination of the AC and specified composition of HEA NPs can generate more active sites to accelerate the transfer of electrons. The reaction channels of the AC promote the migration of dye molecule to HEA NPs. Although the specific surface area slightly decreases (Fig. 2), the loaded HEA NPs significantly improve catalytic efficiency, which discloses a critical role of the HEA NPs along with the redox process.
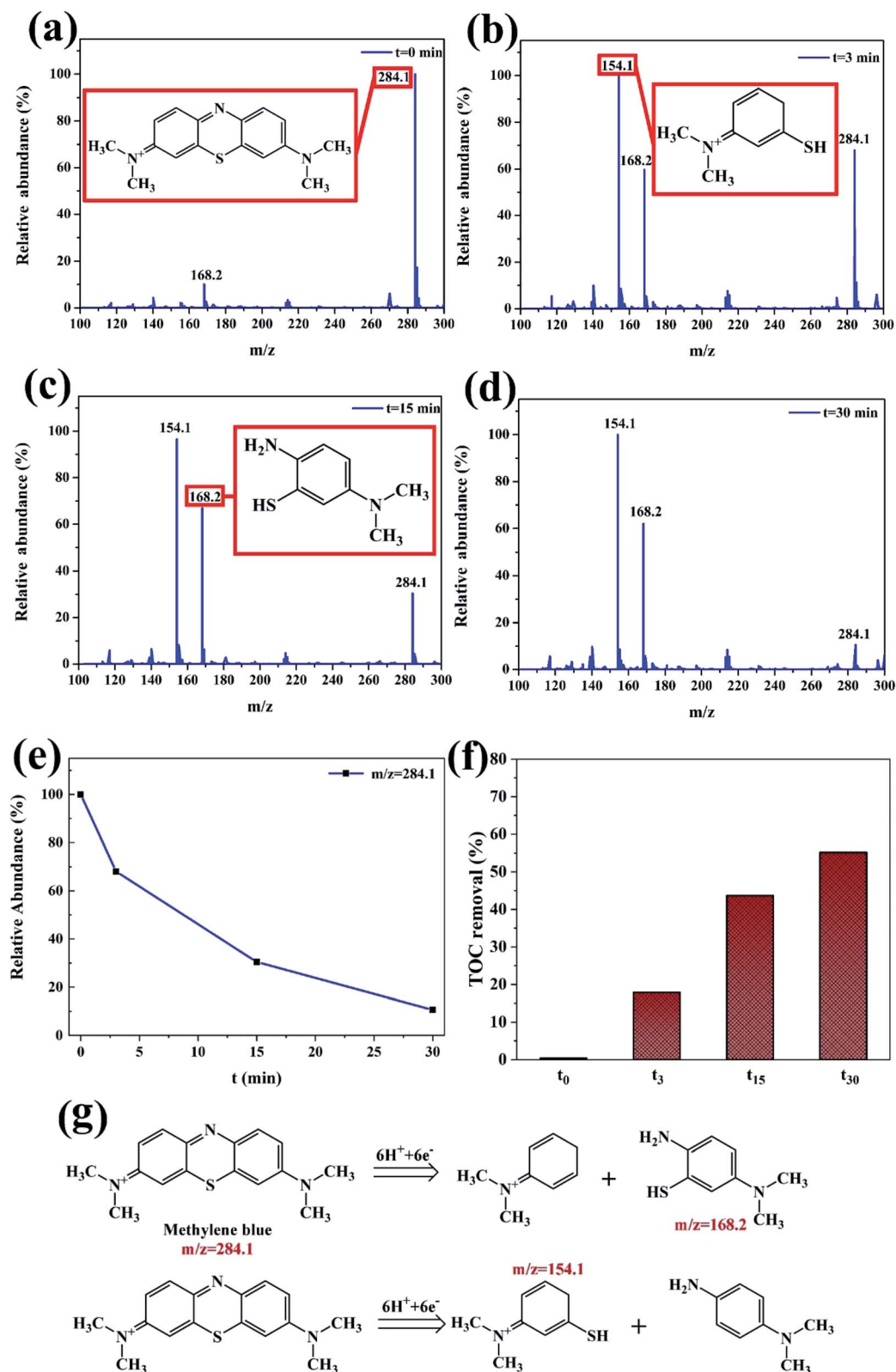
Fig. 10   HRMS analysis for the CoCrFeMnNi HEA NPs−AC at different degradation intervals. (a) t = 0 min, (b) t = 3 min, (c) t = 15 min, (d) t = 30 min, (e) t = 30 min, (e) relative abundance of m/z = 284.1 at different time, (f)TOC at different time, (g) two possible degradation pathways of the MB in the CoCrFeMnNi HEA NPs−AC system.
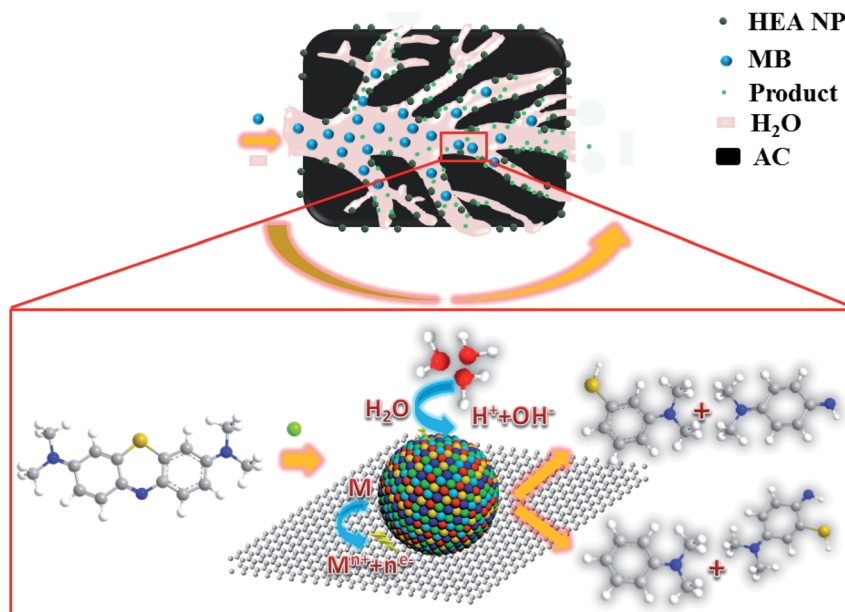
Fig. 11 Schematic diagram for synthesis of the HEA NPs–AC and catalytic reaction mechanism of MB (M refers to HEA NP).

3.4.3. Nanoscale galvanic-cell effect. As shown in Fig. 4, CoCrFeMnNi HEA NPs presented specific features with a number of distinct boundaries and contact with surrounding phases and the heterostructure of AC improve the conductivity of the nanostructure as well, leading to the formation of micro-sized galvanic cells due to potential difference.[37,38] The migration of electrons partly depends on a correlation of electron carrier and transportation in the catalytic reaction. Thus, this potential phase act as the driving force with different phases of the HEA NPs as the dominant electron donors to lose electrons (Fig. 11). Meanwhile, H_2O provides H^+ and OH^-. Large amounts of HEA NPs as nanoscale galvanic cells embedding in distinctive nanoporous architectures have giant advantages in the decomposition of the MB dye by accelerating the electron transfer and mass transport.

4. Conclusion

The nanocomposites of the HEA NPs–AC were fabricated from precursor solution by a facile and scalable impregnation–adsorption method *via* thermal pyrolysis conditions for efficient dye degradation without peroxides. The main conclusions are as follows.

1. The CoCrFeMnNi HEA NPs consist of the single FCC phase and uniformly disperse with average diameter of 89 nm. Specific surface area of the composites decreases with growing loading of HEA NPs. The combination of homogeneous phase formation with distinctive porous architectures provides solid foundation for preeminent catalytic.

2. Adding 10 wt% CoCrFeMnNi HEA NPs/AC, the time required to reduce MB concentration to less than 15% without the addition of peroxides can be as short as 12 minutes with the k_{obs} of 0.191 min^{-1}. Under the same condition (10 wt%), the order of decomposition efficiency for these catalysts is:

CoCrFeMnNi > Fe > Mn > Al > AC. Meanwhile it is also competitive among other catalysts for dye degradation.

3. Large amounts of HEA NPs as nanoscale galvanic cells embedding in distinctive porous architectures have advantages in the decomposition of the MB dye by accelerating the electron transfer and the mass transport.

The nanocomposites of the HEA NPs–AC are distinguished by noble metal-free and high catalytic performance with porous nanostructure, achieving prospective performance in industrial catalytic applications due to the synergetic degradation. This work provides a novel approach to synthesize HEA NPs and expands its promising catalytic application as environmentally friendly materials.

Conflicts of interest

There are no conflicts to declare.

Acknowledgements

References

1 J. W. Yeh, S. K. Chen, S. J. Lin, J. Y. Gan, T. S. Chin, T. T. Shun, C. H. Tsau and S. Y. Chang, *Adv. Eng. Mater.*, 2004, **6**, 299–303.

2 B. Cantor, *Entropy*, 2014, **16**, 4749–4768.

3 Z. Lei, X. Liu, Y. Wu, H. Wang, S. Jiang, S. Wang, X. Hui, Y. Wu, B. Gault, P. Kontis, D. Raabe, L. Gu, Q. Zhang, H. Chen, H. Wang, J. Liu, K. An, Q. Zeng, T.-G. Nieh and Z. Lu, *Nature*, 2018, **563**, 546.

4 Y. Lu, X. Gao, Y. Dong, T. Wang, H. L. Chen, H. Maob, Y. Zhao, H. Jiang, Z. Cao, T. Li and S. Guo, *Nanoscale*, 2018, **10**, 1912–1919.

5 Y. Lu, X. Gao, L. Jiang, Z. Chen, T. Wang, J. Jie, H. Kang, Y. Zhang, S. Guo, H. Ruan, Y. Zhao, Z. Cao and T. Li, *Acta Mater.*, 2017, **124**, 143–150.

6 Y. G. Yao, Z. N. Huang, P. F. Xie, S. D. Lacey, R. J. Jacob, H. Xie, F. J. Chen, A. M. Nie, T. C. Pu, M. Rehwoldt, D. W. Yu, M. R. Zachariah, C. Wang, R. Shahbazian-Yassar, J. Li and L. B. Hu, *Science*, 2018, **359**, 1489–1494.

7 P. C. Chen, X. Liu, J. L. Hedrick, Z. Xie, S. Wang, Q.-Y. Lin, M. C. Hersam, V. P. David and C. A. Mirkin, *Science*, 2016, **352**, 1565–1569.

8 M. Takahashi, H. Koizumi, W.-J. Chun, M. Kori, T. Imaoka and K. Yamamoto, *Sci. Adv.*, 2017, **3**, e1700101.

9 N. A. Frey, S. Peng, K. Cheng and S. H. Sun, *Chem. Soc. Rev.*, 2009, **38**, 2532–2542.

10 Y. F. Ye, Q. Wang, J. Lu, C. T. Liu and Y. Yang, *Mater. Today*, 2015, **19**, 349–362.

11 T. Löffler, H. Meyer, A. Savan, P. Wilde, A. Garzón Manjón, Y.-T. Chen, E. Ventosa, C. Scheu, A. Ludwig and W. Schuhmann, *Adv. Energy Mater.*, 2018, **8**, 1802269.

12 J. Zhou, X. Li, X. Ma, W. Sheng and X. Lang, *Appl. Catal., B*, 2021, **296**, 120368.

13 A. Fujishima, X. Zhang and D. A. Tryk, *Surf. Sci. Rep.*, 2008, **63**, 515–582.

14 K. Deekshitha Vidya Shetty, *Mater. Sci. Semicond. Process.*, 2021, **132**, 105923.

15 Y. Wang, N. Bi, H. Zhang, W. Tian, T. Zhang, P. Wu and W. Jiang, *Colloids Surf., A*, 2020, **585**, 124105.

16 V. P. Singh, M. Sharma and R. Vaish, *Mater. Chem. Phys.*, 2020, **252**, 123311.

17 Z. Han, J. Fei, J. Li, Y. Deng, M. Lv, J. Zhao, C. Wang and X. Zhao, *Chem. Eng. J.*, 2021, **407**, 127214.

18 S. X. Liang, Z. Jia, W. C. Zhang, X. F. Li, W. M. Wang, H. C. Lin and L. C. Zhang, *Appl. Catal., B*, 2018, **221**, 108–118.

19 S. H. Xie, P. Huang, J. J. Kruzic, X. R. Zeng and H. X. Qian, *Sci. Rep.*, 2016, **6**, 21947.

20 Z. Y. Lv, X. J. Liu, B. Jia, H. Wang, Y. Wu and Z. P. Lu, *Sci. Rep.*, 2016, **6**, 34213.

21 S. K. Wu, Y. Pan, J. Lu, N. Wang, W. J. Dai and T. Lu, *J. Mater. Sci. Technol.*, 2019, **35**, 1629–1635.

22 X. Ke, X. Qin, X. Wang, Y. Wang, H. Tao, Q. Wu, L. Yang and Z. Hu, *Adv. Mater.*, 2012, **24**, 347–352.

23 Z. Y. Lyu, D. Xu, L. J. Yang, R. C. Che, R. Feng, J. Zhao, Y. Li, Q. Wu, X. Z. Wang and Z. Hu, *Nano Energy*, 2015, **12**, 657–665.

24 J. Zhao, H. Lai, Z. Lyu, Y. Jiang, K. Xie, X. Wang, Q. Wu, L. Yang, Z. Jin and Y. Ma, *Adv. Mater.*, 2015, **27**, 3541–3545.

25 Z. Y. Jin, J. Lv, H. L. Jia, W. H. Liu, H. L. Li, Z. H. Chen, X. Lin, G. Q. Xie, X. J. Liu, S. H. Sun and H. J. Qiu, *Small*, 2019, **15**, 1904180.

26 K. Shen, X. Chen, J. Chen and Y. Li, *ACS Catal.*, 2016, **6**, 5887–5903.

27 R. Coll, J. Salvadó, X. Farriol and D. Montané, *Fuel Process. Technol.*, 2001, **74**, 19–31.

28 Q. Wang, M. Chen, P. Lin, Z. Cui, C. L. Chu and B. Shen, *J. Mater. Chem. A*, 2018, **6**, 10686–10699.

29 J.-Q. Wang, Y.-H. Liu, M.-W. Chen, G.-Q. Xie, D. V. Louzguine-Luzgin, A. Inoue and J. H. Perepezko, *Adv. Funct. Mater.*, 2012, **22**, 2567–2570.

30 N. Ruiz, S. Seal and D. Reinhart, *J. Hazard. Mater.*, 2000, **80**, 107–117.

31 A. M. Moore, C. H. De Leon and T. M. Young, *Environ. Sci. Technol.*, 2003, **37**, 3189–3198.

32 H. Wang, Q. Yao, C. Wang, B. Fan, Q. Sun, C. Jin, Y. Xiong and Y. Chen, *Sci. Rep.*, 2016, **6**, 35549.

33 Z. Jia, J. Kang, W. C. Zhang, W. M. Wang, C. Yang, H. Sun, D. Habibi and L. C. Zhang, *Appl. Catal., B*, 2017, **204**, 537–547.

34 Z. Wang, W. Qiu, Y. Yang and C. T. Liu, *Intermetallics*, 2015, **64**, 63–69.

35 M. Mavrikakis, B. Hammer and J. Nørskov, *Phys. Rev. Lett.*, 1998, **81**, 2819–2822.

36 Y. E. Seidel, A. Schneider, Z. Jusys, B. Wickman, B. Kasemo and R. J. Behm, *Faraday Discuss.*, 2008, **140**, 167–184.

37 S. Q. Chen, G. N. Yang, S. T. Luo, S. J. Yin, J. L. Jia, Z. Li, S. G. Gao, Y. Shao and K. F. Yao, *J. Mater. Chem. A*, 2017, **5**, 14230–14240.

38 L. Yang, Y. L. Lv and D. P. Cao, *J. Mater. Chem. A*, 2018, **6**, 3926–3932.

39 Z. Xiong, B. Lai, P. Yang, Y. Zhou, J. Wang and S. Fang, *J. Hazard. Mater.*, 2015, **297**, 261–268.

40 B. Kakavandi and A. A. Babaei, *RSC Adv.*, 2016, **6**, 84999–85011.

41 Y. Tang, Y. Shao, N. Chen, X. Liu, S. Q. Chen and K. F. Yao, *RSC Adv.*, 2015, **5**, 34032–34039.

42 Y. Tang, Y. Shao, N. Chen and K.-F. Yao, *RSC Adv.*, 2015, **5**, 6215–6221.